

Strain-induced enhancement of T_c in infinite-layer $\text{Pr}_{0.8}\text{Sr}_{0.2}\text{NiO}_2$ films

Xiaolin Ren^{1,2}, Wei-Chih Chen³, Jiarui Li⁴, Qiang Gao¹, Joshua Sanchez⁴, Hailan Luo^{1,2}, Fanny Rodolakis⁵, Jessica L. McChesney⁵, John W. Freeland⁵, Tao Xiang^{1,2,6}, Jiangping Hu^{1,2,6}, Riccardo Comin⁴, Yao Wang^{3,*}, X. J. Zhou^{1,2,6,7,*}, and Zhihai Zhu^{1,2,7,*}

¹*Institute of Physics, National Laboratory for Condensed Matter Physics, Chinese Academy of Sciences, Beijing 100190, China*

²*School of Physical Sciences, University of Chinese Academy of Sciences, Beijing 100049, China*

³*Department of Physics and Astronomy, Clemson University, Clemson, SC 29631, USA*

⁴*Department of Physics, Massachusetts Institute of Technology, Cambridge, Massachusetts 02139, USA*

⁵*X-Ray Science Division, Advanced Photon Source, Argonne National Laboratory, Lemont, IL 60439, USA*

⁶*Beijing Academy of Quantum Information Sciences, Beijing 100193, China*

⁷*Songshan Lake Materials Laboratory, Dongguan 523808, China*

*To whom correspondence should be addressed. Emails :yaowang@g.clemson.edu, XJZhou@iphy.ac.cn, zzh@iphy.ac.cn

(Dated: March 10, 2022)

Unconventional superconductivity in correlated materials remains a mystery in condensed matter and a key to energy applications. The recent discovery of superconductivity in infinite-layer nickelates, as analog to high- T_c cuprates, has motivated a promising route towards the pairing mechanism. By growing 8 nm $\text{Pr}_{0.8}\text{Sr}_{0.2}\text{NiO}_2$ films on the $(\text{LaAlO}_3)_{0.3}(\text{Sr}_2\text{AlTaO}_6)_{0.7}$ substrate, we successfully raise the transition temperature T_c from 9 K in the widely studied SrTiO_3 -substrated nickelates into 15 K. Then we combine X-ray absorption spectroscopy with first-principle and many-body simulations, revealing the correlation between T_c and the pre-edge peak intensity and further attributing it to the $p-d$ hybridization between Ni and O ligand induced by the strain. The striking difference demonstrates the possibility to enhance unconventional superconductivity by structure engineering and provides a perspective on its pairing mechanism.

High- T_c superconductivity was one of the greatest surprises in quantum materials, which motivated advances in condensed matter theory and enabled applications in power transmission, clean energy, and medical imaging. Due to the complexity stemming from multiple intertwined orders, the pairing mechanism of cuprates remains an enigma [1]. Both microscopic and phenomenological theories have proposed that the unconventional superconductivity is associated with the correlation nature of the d -orbital electrons, active in transition-metal oxides (TMOs) [2, 3]. Phenomenologically, such a correlation effect can be characterized by the Mott insulating parent phase at half-filling, which partially motivated the discovery of magic-angle twisted bilayer graphene [4]. However, this picture fails to answer why the ambient-pressure high T_c occurs only at cuprate instead of its analogs (e.g., iridates and ruthenates). On the microscopic level, the state-of-the-art numerical simulations also raised the debate on whether a long-range ordered superconducting phase exists in the single-band Hubbard model when it approaches the 2D thermodynamic limit [5, 6].

The recent discovery of superconducting nickelates provides a new perspective to this puzzle [7–12]. Due to nickelates’ structural and chemical similarities with cuprates, a comparative study of these two material systems may reveal the dominant pairing mechanism and guide the design of materials with higher T_c [13–23]. Compared to cuprates, although similar magnons or paramagnons have been identified in infinite-layer nickelates with bandwidth of the same order of magnitude

[24–26], a remarkable difference is that the latter exhibit much lower T_c [27–29]. A possible and phenomenological explanation to this lower T_c is that the nickelates RNiO_2 ($R = \text{La}, \text{Pr}, \text{and Nd}$) are Mott-Hubbard insulators according to Zaanen–Sawatzky–Allen classification [19, 22, 30, 31], while cuprates are charge-transfer insulators, manifest as a prominent pre-peak in O K-edge x-ray absorption spectrum (XAS) and usually referred as the Zhang-Rice peak. Given that the charge-transfer energy was also found to anti-correlate with T_c in various cuprate compounds [32, 33], it is conceivable that the oxygen-orbital components of valence electrons may play a crucial role in the pairing mechanism. To test this postulate, a critical step is to manipulate the charge-transfer extent of nickelates and demonstrate the possibility to enhance the superconducting T_c [34–36].

Here, we report a striking enhancement of $T_c^{\text{(onset)}}$ by growing the $\text{Pr}_{0.8}\text{Sr}_{0.2}\text{NiO}_2$ film on a compressive substrate $(\text{LaAlO}_3)_{0.3}(\text{Sr}_2\text{AlTaO}_6)_{0.7}$ (LSAT). Combining first-principle and many-body simulations, we reveal that the in-plane compressive strain strengthens the $p-d$ hybridization between oxygen and Ni^{1+} cations. Thus, a portion of doped carriers distribute into oxygen orbitals, increasing the pre-peak in the oxygen K-edge XAS and being successfully verified by our experiments. This agreement demonstrates the dominant role of the charge-transfer nature in superconductivity and motivates an efficient approach to further enhance superconductivity TMOs. It also hints that low-energy excitations associated with oxygen p -orbitals may be crucial for the ex-

tremely high T_c in cuprates.

SUBSTRATE-INDUCED STRAIN AND ENHANCED T_c

As illustrated in Fig. 1a, b, we prepared $\text{Pr}_{0.8}\text{Sr}_{0.2}\text{NiO}_2$ films of equal thickness 8 nm on two different substrates, SrTiO_3 and LSAT, using pulsed laser deposition (PLD) followed by a CaH_2 -assisted chemical reduction method. Fig. 1c, d show the high-angle annular dark-field (HADF) scanning transmission electron microscopy (STEM) images of the two superconducting $\text{Pr}_{0.8}\text{Sr}_{0.2}\text{NiO}_2$ films on SrTiO_3 and LSAT substrates, respectively. The contrast difference of diffraction spots reveal the uniform growth of the films with an ordered structure of coherent infinite layer, displaying no evidence of minority phases. The well-defined infinite-layer phase of the $\text{Pr}_{0.8}\text{Sr}_{0.2}\text{NiO}_2$ films is further disclosed in the annular bright field (ABF) STEM images in Fig. 1e, h. The clear and sharp interfaces between the films and the substrates confirm that the films are epitaxially strained on the substrates. Besides, the reciprocal space maps (RSM) around the (103) reflection demonstrate that the films are strained to the substrates (see the Supplemental Material for details). Based on both measurements, the in-plane lattice constants of the nickelate films highly match those of the substrates, yielding $\sim 1\%$ compressive in-plane strain in the films grown on LSAT compared to SrTiO_3 .

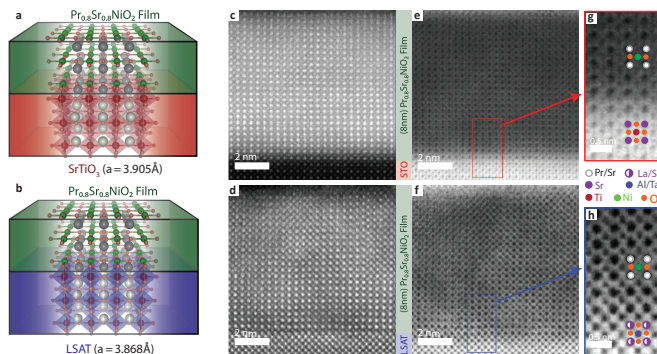


FIG. 1. **Cross-sectional scanning transmission electron microscopy (STEM) images of two typical superconducting $\text{Pr}_{0.8}\text{Sr}_{0.2}\text{NiO}_2$ films on SrTiO_3 and LSAT substrates.** a, b, The schematic illustrations of heterostructures of $\text{Pr}_{0.8}\text{Sr}_{0.2}\text{NiO}_2$ films on two different substrates SrTiO_3 and LSAT, respectively. c, d, The high-angle annular dark field (HADF) STEM images of films on SrTiO_3 and LSAT substrates, respectively. e, f, The annular bright field (ABF) STEM images of film on SrTiO_3 and LSAT substrates, respectively. g, h, The enlarged views of the areas inside the rectangles in e and f, respectively.

With the nickelate films on distinct substrates, we first examine their transport properties using a Quantum

Design Physical Property Measurement System (PPMS) with a standard four-probe configuration. Fig. 2a shows the temperature-dependent resistivity of these two typical $\text{Pr}_{0.8}\text{Sr}_{0.2}\text{NiO}_2$ films on SrTiO_3 and LSAT substrate, respectively. Both films exhibit a sudden decrease of resistivity, characteristic of the superconducting transition. Here, we employ the onset temperature to quantify the superconductivity critical temperature T_c , resulting in $T_c^{(\text{onset})} = 9$ K and 15 K (highlighted with arrow) for samples grown on SrTiO_3 and LSAT, respectively. To further confirm the superconducting behavior, we investigate the transport properties with a magnetic field (up to 9.0-tesla) applied perpendicular to the ab -plane of the film. As shown in Fig. 2c, d, the field dependence exhibits similar behaviors: In the normal state, the films display negligible variation, whereas, below the superconducting transition, the conductance is suppressed significantly with increasing magnetic field.

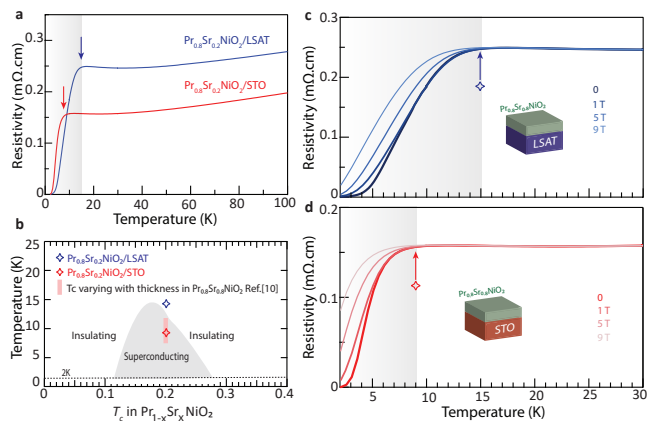


FIG. 2. **Transport properties and magnetic-field response of superconducting $\text{Pr}_{0.8}\text{Sr}_{0.2}\text{NiO}_2$ films on SrTiO_3 and LSAT substrates.** a, Temperature-dependent resistivity of the $\text{Pr}_{0.8}\text{Sr}_{0.2}\text{NiO}_2$ on SrTiO_3 and LSAT substrates, respectively. b The phase diagram of $\text{Pr}_{1-x}\text{Sr}_x\text{NiO}_2$ films adapted from Ref.[11]. The T_c varying from 7 K to 12 K with thickness for $\text{Pr}_{0.8}\text{Sr}_{0.2}\text{NiO}_2$ films adapted from Ref.[10] (pink bar). The $T_c^{(\text{onset})} \approx 9$ K (red diamond) and $T_c^{(\text{onset})} \approx 15$ K (blue diamond) of our 8 nm-thick uncapped $\text{Pr}_{0.8}\text{Sr}_{0.2}\text{NiO}_2/\text{SrTiO}_3$ and $\text{Pr}_{0.8}\text{Sr}_{0.2}\text{NiO}_2/\text{LSAT}$. c, d Magnetic-field response of superconducting $\text{Pr}_{0.8}\text{Sr}_{0.2}\text{NiO}_2$ film on SrTiO_3 and LSAT substrates, at a varying magnetic field perpendicular to the a - b plane. The onset of superconducting transition at 9 K for the film on SrTiO_3 is smaller than that of the film at 15 K on LSAT substrate. Zero-resistance is obtained respectively at 2.5 K and 2.0 K for the films on LSAT and SrTiO_3 .

We summarize the critical temperatures of various nickelate experiments by the gray area in Fig. 2b to compare with previous experiments. Considering the sensitivity to the thickness, we further mark the T_c varying from 7 K to 12 K with respect to thickness for $\text{Pr}_{0.8}\text{Sr}_{0.2}\text{NiO}_2$ films [10]. The $T_c^{(\text{onset})} \approx 9$ K (denoted by the red diamond) of our 8 nm-thick uncapped

$\text{Pr}_{0.8}\text{Sr}_{0.2}\text{NiO}_2$ film grown on SrTiO_3 is lower than that $T_c^{(\text{onset})} \approx 12$ K from the previous studies on the film with equal thickness. Interestingly, when substrated by LSAT, the same uncapped 8 nm-thick $\text{Pr}_{0.8}\text{Sr}_{0.2}\text{NiO}_2$ film exhibits a considerably higher $T_c^{(\text{onset})} \approx 15$ K, beyond the record of any (capped and uncapped) STO-substrated samples for the same doping. Admittedly, the uncapped films on both substrates in our study show a relatively larger broadening of superconducting transition, which is probably due to the detailed topotactic reduction and common in various superconducting nickelate films [12, 37]. Nevertheless, in Fig. 2a the zero-resistance is respectively achieved at $T_c^{(\text{zero})} = 2.0$ K and 2.5 K in zero-field for the films on SrTiO_3 and LSAT. We caution that T_c is contingent upon the details of film growth and topotactic reduction, and can vary significantly. We emphasize that in our comprehensive optimal procedure the observation of $T_c^{(\text{onset})}$ enhancement for equally thick films on LSAT compared to SrTiO_3 is robust. Since the interfacial effects should be irrelevant for 8 nm-thick nickelates, we attributed this dramatic $T_c^{(\text{onset})}$ enhancement in the comparative study to the crystal structure of $\text{Pr}_{0.8}\text{Sr}_{0.2}\text{NiO}_2$, which is compressively strained by the LSAT substrate.

PRE-EDGE PEAK IN X-RAY ABSORPTION SPECTRA

To unveil the connection between the strain and the enhancement of T_c in $\text{Pr}_{0.8}\text{Sr}_{0.2}\text{NiO}_2/\text{LSAT}$, we further examine their electronic structure using XAS. We select the O K -edge to reveal the nature of dopant carriers, since its characteristic peaks have been regarded as a fingerprint in cuprates. Similar to other recent studies, we find that the K -edge XAS of $\text{Pr}_{0.8}\text{Sr}_{0.2}\text{NiO}_2$ exhibits only a single peak near the edge (531 eV), identified as the upper Hubbard band (UHB) [22, 38]. The absence or negligible weight of any pre-edge peak suggests that the parent compound of superconducting nickelates ($\text{Pr}_{0.8}\text{Sr}_{0.2}\text{NiO}_2/\text{SrTiO}_3$) fall into the Mott-Hubbard type regime. This is in sharp contrast to cuprates, where an extra pre-edge mobile carrier peak (MCP) arises with hole doping and carries intensity comparable with the doping concentration. We illustrate the difference in XAS features via the partial density of states (PDOS) distribution sketched in Fig. 3c. As charge-transfer insulators, cuprates have a relatively strong on-site Coulomb interaction U_d (primarily for the Cu $3d$ electrons) compared to the charge-transfer energy Δ_h of a hole. Therefore, a doped hole primarily occupies the oxygen $2p$ orbital, which hybridizes with the Cu $3d$ orbital as the ‘‘Zhang-Rice’’ singlet band. XAS selectively probes the unoccupied PDOS on oxygen, resulting in the coexistence of the pre-edge MCP and the UHB peaks. Nevertheless, the Δ_h is slightly larger than the U_d on nickelates, leading to tiny, if any, dopant holes

residing on oxygen orbitals and, accordingly, a single absorption peak. This difference between charge-transfer and Mott-Hubbard insulators is exact only in the atomic limit, while the presence of orbital hybridization mixes them (see the SI for detailed discussions).

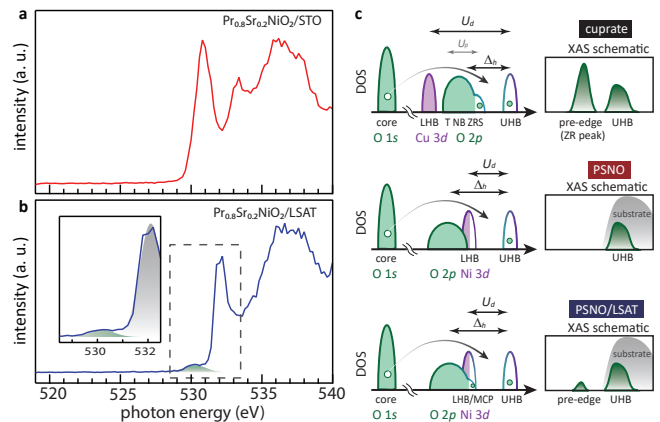


FIG. 3. Total fluorescence yield X-ray absorption spectra (XAS) of $\text{Pr}_{0.8}\text{Sr}_{0.2}\text{NiO}_2$ thin films with the linear polarization perpendicular to the films’ c axis. a, b, The XAS at the O K edge of PSNO/STO and PSNO/LSAT. The inset in b is the enlarged view of the area inside of the dot lines and it shows a clearly visible pre-edge peak, reflecting the emergence of the mobile carrier peak (MCP) that, however, is absent in the film on SrTiO_3 substrate. c, Schematic electronic structure of the XAS experiment.

Unlike the STO-substrated nickelates, the XAS spectrum of our $\text{Pr}_{0.8}\text{Sr}_{0.2}\text{NiO}_2/\text{LSAT}$ sample exhibits an evident pre-peak at the O K main edge at 530.2 eV, reminiscent of the pre-peaks in cuprates [39]. The energy position of 530.2 eV for the pre-peak is nearly equal to the observed hybridization peak in $\text{La}_4\text{Ni}_3\text{O}_8$, which belongs to another family of nickelate materials ($\text{R}_{n+1}\text{Ni}_n\text{O}_{2n+2}$) [40]. Therefore, we can tentatively attribute this pre-edge peak in $\text{Pr}_{0.8}\text{Sr}_{0.2}\text{NiO}_2/\text{LSAT}$ to the MCP. Since the charge-transfer nature appears to be one of the most significant differences between cuprates and nickelates, the emergence of the pre-edge XAS peak in LSAT-substrated nickelates provides insight for its enhanced T_c .

NUMERICAL EXPLANATION OF THE ELECTRONIC STRUCTURE’S CHANGE

To reveal the impact of the strained lattice on nickelates’ electronic structure, we simulate the doped carriers and spectral evolution upon straining using density functional theory (DFT) and the extracted many-body model. We first calculate the electronic structure of the pristine and -1% strained PSNO using PBE functional (see Methods). As shown in Fig. 4, the simulated PDOS reflects that HOMO and LUMO orbitals primarily consist of Ni $3d_{x^2-y^2}$ orbitals. As pointed out by

previous studies [22], the rare-earth band also resides at low energy, leading to a “self-doping” effect. To address the experimental features observed in the oxygen K-edge XAS, we particularly focus on the oxygen components of low-energy electrons. By projecting the simulated Kohn-Sham orbitals to the single-particle Wannier orbitals, we extracted two oxygen orbitals ($2p_x$ and $2p_y$) which hybridize with the active Ni $3d_{x^2-y^2}$ orbital [see the inset]. To analyze the electronic structure associated with the oxygen orbitals, we employ these three orbitals to construct a tight-binding model, Eq. (1) in the Method section, where the hopping parameters is extracted from the Kohn-Sham Wannier orbitals. For the pristine PSNO, we obtain $t_{pd} = 1.36$ eV, $t_{pp} = 0.57$ eV, and $E_d - E_p = 3.90$ eV consistent with previous simulations [22]; for the -1% strained PSNO, t_{pd} are evidently increased into 1.41 eV, while the changes of other parameters are less than 2%.

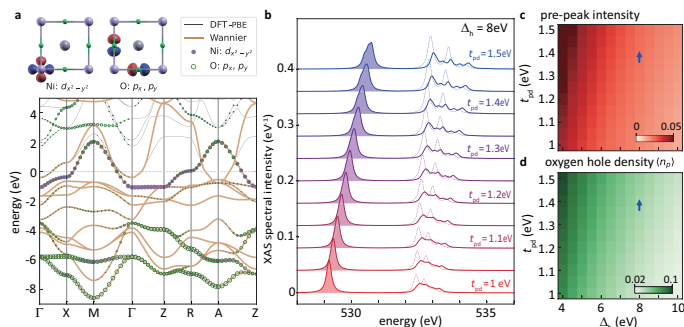


FIG. 4. Theoretical modeling of $\text{Pr}_{0.8}\text{Sr}_{0.2}\text{NiO}_2$ based on density functional theory (DFT), Wannier functions, and exact diagonalization X-ray absorption spectroscopy. **a**, Band structures of unstrained PrNiO_2 from DFT and Wannier tight-binding model. Nickel’s $d_{x^2-y^2}$ and oxygen’s p_x and p_y orbitals are shown on the top, where gray, purple, and green spheres represent Pr, Ni, and O, respectively. The site energies of E_d and E_p , as well as the hopping parameters t_{pd} (hopping between Ni: $d_{x^2-y^2}$ and O: p_x, p_y) and t_{pp} (hopping between O: p_x and p_y) in Wannier tight-binding model are extracted using Wannier90 package. These parameters are in turn used in our exact diagonalization modeling. **b**, Exact diagonalization X-ray absorption spectra with a $\Delta_h = 8$ eV and a varying t_{pd} from 1.0 eV to 1.5 eV. The prepeak area increases with increasing t_{pd} while the gap between the prepeak and the upper Hubbard band (UHB) decreases with increasing t_{pd} . The prepeak area **c** and the average hole number per $p_{x,y}$ orbital **d** as a function of Δ_h and t_{pd} are shown by the intensity plots. Both of them increase with an increasing t_{pd} and increasing Δ_h . The blue arrows indicate the change of t_{pd} from 1.36 to 1.41 eV when 1 % compressive epitaxial strain is applied while the changes of site energies, E_d and E_p , are negligible.

We then involve the strong Coulomb interactions and x-ray core-hole interactions on top of the DFT-extracted model to simulate the XAS spectra and analyze correlation effects. Based on estimations from previous studies,

we set the Hubbard-type Coulomb interactions on the Ni $3d$ and O $2p$ orbitals as $U_d = 6$ eV and $U_p = 2$ eV, respectively. We also set the core-hole attractive interaction to be $U_c = 3$ eV to match the experimental separation between the pre-edge and main peaks. (The selection of U_c does not change our conclusions.) The XAS spectral intensity is given by Eq. (2) in the Method section. As shown in Fig. 4**b**, we manipulate the strength of t_{pd} and fix other parameters, mimicking the primary impact on the electronic structure induced by the strain effect. Considering possible ambiguities of band parameters extracted from the Kohn-Sham orbitals, we examine the spectral properties for a wide range of t_{pd} values, from 1.0 to 1.5 eV. The simulated XAS results suggest that increased t_{pd} , induced by the compressive strain effect, causes an enhancement of the pre-edge peak, consistent with our experimental observations in Figs. 3**a** and **b**. As illustrated in Fig. 3**c**, although the strain does not switch the relative size of U_d to Δ_h in the atomic representation, the increased t_{pd} causes the mixture of oxygen and nickel PDOS at the top of the LHB. Therefore, a larger portion of the doped holes reside in oxygens, resulting in the rise of the pre-edge XAS peak.

To further demonstrate the mechanism mentioned above, we further calculate the hole concentrations $\langle n_p \rangle$ on the two oxygen orbitals. By comparing the undoped and doped XAS results, it is clear that the pre-edge peak reflects the majority of dopant carrier concentrations in oxygens. Therefore, we evaluate the pre-peak intensity and $\langle n_p \rangle$ for a wide range of charge-transfer energy Δ_h and t_{pd} of the three-band Hubbard model. As shown in Fig. 4**c** and **d**, the parameter dependences of these two quantities exhibit strong correlations in the entire $\Delta_h - t_{pd}$ parameter space. The two ends of the arrows indicate the DFT-extracted model parameters for the pristine and strained PSNO. In this context, the pre-edge peak intensity rises by 2.8%, and the oxygen-hole concentration increases by 3.1%. While the simplicity of the three-band model and the accuracy of the DFT simulated parameters may affect the exact values, the correlation between the spectral and carrier properties qualitatively reflects that the nickelates in LSAT substrate distribute more dopant carriers into oxygen orbitals.

DISCUSSION AND OUTLOOK

The fact that strained PSNO displays a much higher T_c not only provides an efficient route to control, and especially enhance, the superconductivity in nickelates, but also may help reveal the nature of unconventional superconductivity in correlated materials. Since the enhancement of SC is accompanied by the rise of the pre-edge peak, which can be mapped to the carrier concentration in oxygens, it reflects that the TM-oxygen hybridization, or the charge-transfer nature plays a crucial role in the pairing mechanism. One possible explanation to this correlation is that the increase of hybridization increases the

bandwidth of the conduction band, resulting in a larger super-exchange energy $J = 4t^2/U$. According to our first-principle simulation, the bandwidth is increased by 4.2% for a -1% strain, while its impact on T_c remains to be addressed with large-scale numerical simulations [41]. An alternative explanation lies in bosonic modes coupling to oxygen atoms, such as the phonons originating from oxygen vibrations. With more dopant carriers in oxygen orbitals induced by the compressive strain, the low-energy quasiparticles, which dominate the transport properties, are more sensitive to these bosonic modes. Recent studies in cuprates have revealed the presence of non-negligible electron-phonon and suggested that it may be related to the pairing mechanism of high T_c superconductivity [42–46]. Although insights have been obtained via, *e.g.*, the correlation-enhanced polaronic dressing [47] or phonon-mediated attractive interactions [48, 49], the interplay between phonons and strong electronic correlations, as well as their combined impact on unconventional superconductivity, remains to be investigated.

More experimental studies are necessary to further distinguish these two potential mechanisms. If the lattice dressing effects are crucial in the rise of T_c of the strained nickelates, electron-phonon coupling signatures, such as kinks and dip-hump features, should become more evident in angle-resolved photoemission or scanning tunneling spectroscopies. Unfortunately, these surface-sensitive measurements are not accessible at the current state due to the poor surface quality of infinite-layer nickelates resulting from the topotactic reduction. This conflict needs to be reconciled from continuing efforts on improving surface quality of film samples or synthesizing single-crystalline bulk samples. An alternative approach is the resonant inelastic x-ray scattering (RIXS), which has characterized both the magnon and phonon dispersions in STO-substrated $\text{Nd}_{1-x}\text{Sr}_x\text{NiO}_2$ [24]. As the detuning method is likely to characterize the coupling strength [50], the comparison of RIXS measurements of nickelates on these two substrates may provide more insight into the underlying mechanism. Thus, our results pave the way to future studies on the strain-tuning of superconducting properties of the infinite-layer nickelates and ultimately to determine their pairing mechanism.

METHOD

A. Sample Preparation and Experimental Characterization

The perovskite precursor $\text{Pr}_{0.8}\text{Sr}_{0.2}\text{NiO}_3$ films were prepared by using pulsed laser deposition (PLD). The corresponding infinite-layer phase was acquired by soft-chemistry reduction method. The superconducting transition temperature was confirmed by transport measurements using a Quantum Design Physical Property Measurement System (PPMS) with a standard four-probe configuration. Samples for the cross-sectional scanning

transmission electron microscopy (STEM) were prepared by focused ion beam (FIB, Helios 600i) techniques. The high-angle annular dark field (HAADF) and annular bright field (ABF) STEM images were acquired on the ARM-200F (JEOL, Japan) operated at 200 kV with a CEOS Cs corrector (CEOS GmbH, Germany). The x-ray absorption spectroscopy (XAS) measurements were performed at beamline 29-ID IEX at the Advanced Photon Source, Argonne National Laboratory. The beamline uses an electromagnetic undulator providing a soft x-ray from 250 eV to 3000 eV. The spectra were normalized by the incident x-ray intensity (I0) using a drain current from a gold mesh upstream of the sample. All spectra were collected at 30K.

B. Density Functional Theory Calculations

The electronic band structure of PrNiO_2 is calculated using Quantum Espresso package with Perdew-Burke-Ernzerhof (PBE) exchange-correlation functional, where the pseudopotential is based on projected augmented wave (PAW) method. We adopt the Monkhorst-Pack sampling with a Γ -centered k-mesh of $13 \times 13 \times 15$ and a plane-wave cutoff energy of 40 rydberg is used to expand the wavefunction. The convergence criteria of structure relaxation and self-consistent field are set to 10^{-4} rydberg/bohr and 10^{-7} rydberg, respectively. For the -1 % strained structure, we then change the lengths of a- and b-axis directly while c-axis remains unchanged.

To extract the site energies and hopping parameters, we employ Wannier90 package to fit our DFT results and construct the tight-binding models, where a total number of 16 Wannier functions: five Pr's d orbitals, five Ni's d orbitals, and six O's p orbitals, are considered. In our calculations, the disentanglement procedure is employed with a disentanglement window from -10 to +0.8 eV.

Exact Diagonalization Simulation for XAS Spectra

We employ the three-band Hubbard model extracted from the DFT Wannier orbitals as a minimal description of the charge-transfer physics in PSNO. The Hamiltonian reads as:

$$\begin{aligned} \mathcal{H}_v = & - \sum_{\langle i,j \rangle \alpha \sigma} t_{pd}^{ij} \left(d_{i\sigma}^\dagger p_{j\alpha\sigma} + h.c. \right) \\ & - \sum_{\langle j,j' \rangle \sigma} t_{pp}^{jj'} \left(p_{jx\sigma}^\dagger p_{j'y\sigma} + h.c. \right) + \sum_{i\sigma} E_d n_{i\sigma}^d + \sum_{j\alpha\sigma} E_p n_{j\alpha\sigma}^p \\ & + \sum_i U_d n_{i\uparrow}^d n_{i\downarrow}^d + \sum_{j\alpha} U_p n_{j\alpha\uparrow}^p n_{j\alpha\downarrow}^p. \end{aligned} \quad (1)$$

Here, $d_{i\sigma}^\dagger$ ($p_{j\alpha\sigma}^\dagger$) creates an electron with spin σ at a Ni site i (O site j), and $n_{i\sigma}^d$ ($n_{j\alpha\sigma}^p$) is the Ni (O) electron number. The flavor $\alpha = \{x, y\}$ labels the $2p_{x,y}$ orbitals. The

t_{pd} and t_{pp} determines the nearest-neighbor hopping amplitudes and E_d (E_p) is the electronic site energy. These single-particle parameters are extracted from the Wannier orbitals of the DFT simulation. The last two terms are the on-site Hubbard interactions, whose strengths are set as *ad hoc* parameters $U_d = 6$ eV, $U_p = 2$ eV, comparable with previous literatures [22, 31]. The charge-transfer energy in the hole representation is defined as $\Delta_h = E_d - E_p + U_d - U_p$. At the pristine PSCO, the DFT simulation gives $\Delta_h=8$ eV, $|t_{pd}| = 1.36$ eV, $|t_{pp}| = 0.57$ eV, while in the -1% strained PSCO, the extracted parameters of $|t_{pd}|$ and $|t_{pp}|$ are =1.41 eV and 0.58 eV. We perform exact diagonalization calculations of the XAS spectrum of a the three-band Hubbard model on an 8-site cluster for two different doping levels: 0 % (half-filling) and 12.5 % (underdoped).

With the many-body ground state $|G\rangle$, the zero-temperature XAS spectrum is

$$I_{\text{XAS}}(\omega, T) = -\frac{1}{\pi} \text{Im} \langle G | \mathcal{D}^\dagger \frac{1}{\omega + E_G - \mathcal{H} + i\delta} \mathcal{D} | G \rangle \quad (2)$$

where E_G is the ground-state energy and δ is the broadening corresponding to the inverse lifetime of the intermediate state. For the convenience of extracting the integrated peak intensity, we employed a small broadening $\delta = 0.1$ eV in the simulation, where realistic values should be much larger. The dipole operators \mathcal{D} define the transformation between the oxygen 1s (core-level) and the 2p orbitals (valence level) selected by the x-ray K -edge edge

$$\mathcal{D} = A_{O-K} \sum_{\alpha\sigma} p_{j\alpha\sigma}^\dagger c_{j\sigma}. \quad (3)$$

Since we do not compare absolute intensities among dif-

ferent edges, we ignore the matrix element A_{O-K} . In addition to the valence-band tight-binding model \mathcal{H}_v , the intermediate state in Eq.(2) contains an extra core hole and its attractive interaction

$$\mathcal{H}_c = \sum_{i\sigma} E_{\text{edge}} (1 - n_{i\sigma}^c) - U_c \sum_{i\sigma\sigma'} n_{i\sigma}^p (1 - n_{i\sigma'}^c), \quad (4)$$

where E_{edge} is the edge energy $E_{\text{edge}} = 530$ eV and $U_c = 3$ eV the core-hole potential.

Acknowledgement

This work was supported in part by the National Natural Science Foundation of China (Grant No. 12074411) and (Grant No. 11888101), the National Key Research and Development Program of China (Grant No. 2016YFA0300300 and 2017YFA0302900), the Strategic Priority Research Program (B) of the Chinese Academy of Sciences (Grant No. XDB25000000) and the Research Program of Beijing Academy of Quantum Information Sciences (Grant No. Y18G06). The first-principle and model-based spectral simulations used resources of the National Energy Research Scientific Computing Center (NERSC), a U.S. Department of Energy Office of Science User Facility operated under Contract No. DE-AC02-05CH11231. The work performed at the Advanced Photon Source was supported by the U.S. Department of Energy, Office of Science, and Office of Basic Energy Sciences under Contract No. DE-AC02-06CH11357.

-
- [1] Keimer, B., Kivelson, S. A., Norman, M. R., Uchida, S. & Zaanen, J. From quantum matter to high-temperature superconductivity in copper oxides. *Nature* **518**, 179–186 (2015). URL <https://www.nature.com/articles/nature14165>.
- [2] Anderson, P. W. The resonating valence bond state in La_2CuO_4 and superconductivity. *Science* **235**, 1196–1198 (1987). URL <https://www.science.org/doi/10.1126/science.235.4793.1196>.
- [3] Dagotto, E. Correlated electrons in high-temperature superconductors. *Rev. Mod. Phys.* **66**, 763 (1994). URL <https://link.aps.org/doi/10.1103/RevModPhys.66.763>.
- [4] Cao, Y. *et al.* Unconventional superconductivity in magic-angle graphene superlattices. *Nature* **556**, 43–50 (2018). URL <https://www.nature.com/articles/nature26160>.
- [5] Jiang, H. C. & Devereaux, T. P. Superconductivity in the Doped Hubbard Model and Its Interplay with Next-Nearest Hopping T'. *Science* **365**, 1424 (2019). URL <https://www.science.org/doi/10.1126/science.aal5304>.
- [6] Jiang, S., Scalapino, D. J. & White, S. R. Ground State Phase Diagram of the t - t' - J Model. *Proc. Natl. Acad. Sci.* **118**, e2109978118 (2021). URL <https://www.pnas.org/doi/abs/10.1073/pnas.2109978118>.
- [7] Li, D. *et al.* Superconductivity in an infinite-layer nickelate. *Nature* **572**, 624 (2019). URL <https://www.nature.com/articles/s41586-019-1496-5>.
- [8] Li, D. *et al.* Superconducting Dome in $\text{Nd}_{1-x}\text{Sr}_x\text{NiO}_2$ Infinite Layer Films. *Phys. Rev. Lett.* **125**, 6 (2020). URL <https://journals.aps.org/prl/pdf/10.1103/PhysRevLett.125.027001>.
- [9] Zeng, S. *et al.* Phase Diagram and Superconducting Dome of Infinite-Layer $\text{Nd}_{1-x}\text{Sr}_x\text{NiO}_2$ Thin Films. *Phys. Rev. Lett.* **125**, 7 (2020). URL <https://journals.aps.org/prl/pdf/10.1103/PhysRevLett.125.147003>.
- [10] Osada, M. *et al.* A Superconducting Praseodymium Nickelate with Infinite Layer Structure. *Nano Lett.* **20**, 5735–5740 (2020). URL <https://pubs.acs.org/doi/pdf/10.1021/acs.nanolett.0c01392>.
- [11] Osada, M., Wang, B., Lee, K., Li, D. & Hwang, H. Phase diagram of infinite layer praseodymium nickelate $\text{Pr}_{1-x}\text{Sr}_x\text{NiO}_2$ thin films. *Phys. Rev. Mater.* **4**, 5 (2020). URL <https://journals.aps.org/prmaterials/pdf/10.1103/PhysRevMaterials.4.121801>.

- [12] Pan, G. A. *et al.* Superconductivity in a quintuple-layer square-planar nickelate. *Nat. Mater.* **21**, 160 (2022).
- [13] Anisimov, V. I., Bukhvalov, D. & Rice, T. M. Electronic structure of possible nickelate analogs to the cuprates. *Phys. Rev. B* **59**, 7901–7906 (1999). URL <https://link.aps.org/doi/10.1103/PhysRevB.59.7901>.
- [14] Lee, K. W. & Pickett, W. E. Infinite-layer $\text{LaNiO}_2:\text{Ni}^{1+}$ is not Cu^{2+} . *Phys. Rev. B* **70**, 165109 (2004). URL <https://link.aps.org/doi/10.1103/PhysRevB.70.165109>.
- [15] Jiang, P., Si, L., Liao, Z. & Zhong, Z. Electronic structure of rare-earth infinite-layer RNiO_2 ($\text{R} = \text{La}, \text{Nd}$). *Phys. Rev. B* **100**, 5 (2019). URL <https://doi.org/10.1103/PhysRevB.100.020106>.
- [16] Choi, M. Y., Lee, K. & Pickett, W. E. Role of 4f states in infinite-layer NdNiO_2 . *Phys. Rev. B* **101**, 7 (2020). URL <https://journals.aps.org/prb/pdf/10.1103/PhysRevB.101.020503>.
- [17] Botana, A. S. & Norman, M. R. Similarities and Differences between LaNiO_2 and CaCuO_2 and Implications for Superconductivity. *Phys. Rev. X* **10**, 6 (2020). URL <https://journals.aps.org/prx/pdf/10.1103/PhysRevX.10.011024>.
- [18] Wu, X. *et al.* Robust $d_{x^2-y^2}$ -wave superconductivity of infinite-layer nickelates. *Phys. Rev. B* **101**, 5 (2020). URL <https://journals.aps.org/prb/pdf/10.1103/PhysRevB.101.060504>.
- [19] Jiang, M., Berciu, M. & Sawatzky, G. A. Critical Nature of the Ni Spin State in Doped NdNiO_2 . *Phys. Rev. Lett.* **124**, 5 (2020). URL <https://journals.aps.org/prl/pdf/10.1103/PhysRevLett.124.207004>.
- [20] Sakakibara, H. *et al.* Model Construction and a Possibility of Cupratelike Pairing in a New d(9) Nickelate Superconductor (Nd,Sr) NiO_2 . *Phys. Rev. Lett.* **125**, 6 (2020). URL <https://journals.aps.org/prl/pdf/10.1103/PhysRevLett.125.077003>.
- [21] Karp, J. *et al.* Many-Body Electronic Structure of NdNiO_2 and CaCuO_2 . *Phys. Rev. X* **10**, 11 (2020). URL <https://journals.aps.org/prx/pdf/10.1103/PhysRevX.10.021061>.
- [22] Hepting, M. *et al.* Electronic structure of the parent compound of superconducting infinite-layer nickelates. *Nat. Mater.* **19**, 381 (2020). URL <https://www.nature.com/articles/s41563-019-0585-z.pdf>.
- [23] Been, Emily and Lee, Wei-Sheng and Hwang, Harold Y. and Cui, Yi and Zaanen, Jan and Devereaux, Thomas and Moritz, Brian and Jia, Chunjing. Electronic structure trends across the rare-earth series in superconducting infinite-layer nickelates. *Phys. Rev. X* **11**, 011050 (2021). URL <https://link.aps.org/doi/10.1103/PhysRevX.11.011050>.
- [24] Lu, H. *et al.* Magnetic excitations in infinite-layer nickelates. *Science* **373**, 213–216 (2021). URL <https://www.science.org/doi/abs/10.1126/science.abd7726>.
- [25] Rossi, M., Osada, M., Choi, J., Agrestini, S. *et al.* A broken translational symmetry state in an infinite-layer nickelate (2021). URL <https://arxiv.org/abs/2112.02484>.
- [26] Krieger, G. *et al.* Charge and spin order dichotomy in NdNiO_2 driven by SrTiO_3 capping layer (2021). URL <https://arxiv.org/abs/2112.03341>.
- [27] Hayward, M., Green, M., Rosseinsky, M. & Sloan, J. Sodium hydride as a powerful reducing agent for topotactic oxide deintercalation: Synthesis and characterization of the nickel(I) oxide LaNiO_2 . *J. Am. Chem. Soc.* **121**, 8843–8854 (1999). URL <https://doi.org/10.1021/ja991573i>.
- [28] Hayward, M. A. & Rosseinsky, M. J. Synthesis of the infinite layer Ni (I) phase NdNiO_{2+x} by low temperature reduction of NdNiO_3 with sodium hydride. *Solid State Sci.* **5**, 839–850 (2003).
- [29] Zhao, D. *et al.* Intrinsic spin susceptibility and pseudogaplike behavior in infinite-layer lanio_2 . *Phys. Rev. Lett.* **126**, 197001 (2021). URL <https://link.aps.org/doi/10.1103/PhysRevLett.126.197001>.
- [30] Zaanen, J., Sawatzky, G. A. & Allen, J. W. Band gaps and electronic structure of transition-metal compounds. *Phys. Rev. Lett.* **55**, 418–421 (1985). URL <https://link.aps.org/doi/10.1103/PhysRevLett.55.418>.
- [31] Chen, Z. *et al.* Electronic structure of superconducting nickelates probed by resonant photoemission spectroscopy (2022). URL <https://www.sciencedirect.com/science/article/pii/S2590238522000480>.
- [32] Ruan, W. *et al.* Relationship between the parent charge transfer gap and maximum transition temperature in cuprates. *Sci. Bull.* **61**, 1826–1832 (2016). URL <https://www.sciencedirect.com/science/article/pii/S2095927316306168>.
- [33] Weber, C., Yee, C., Haule, K. & Kotliar, G. Scaling of the transition temperature of hole-doped cuprate superconductors with the charge-transfer energy. *EPL (Europhysics Letters)* **100**, 37001 (2012). URL <https://doi.org/10.1209/0295-5075/100/37001>.
- [34] Hirsch, J. & Marsiglio, F. Hole superconductivity in infinite-layer nickelates. *Physica C Supercond* **566**, 1353534 (2019). URL <https://www.sciencedirect.com/science/article/pii/S0921453419303053>.
- [35] Kitatani, M. *et al.* Nickelate superconductors—a renaissance of the one-band Hubbard model. *npj Quantum Mater.* **5**, 6 (2020). URL <https://www.nature.com/articles/s41535-020-00260-y.pdf>.
- [36] Leonov, I. Effect of lattice strain on the electronic structure and magnetic correlations in infinite-layer (Nd,Sr) NiO_2 . *J. Alloys Compd.* **883**, 160888 (2021). URL <https://www.sciencedirect.com/science/article/pii/S0925838821022970>.
- [37] Li, Y. *et al.* Impact of cation stoichiometry on the crystalline structure and superconductivity in nickelates. *Front. Phys.* **9** (2021). URL <https://www.frontiersin.org/article/10.3389/fphy.2021.719534>.
- [38] Rossi, M. and Lu, H. and Nag, A. and Li, D. and Osada, M. and Lee, K. and Wang, B. Y. and Agrestini, S. and Garcia-Fernandez, M. and Kas, J. J. and Chuang, Y. -D. and Shen, Z. X. and Hwang, H. Y. and Moritz, B. and Zhou, Ke-Jin and Devereaux, T. P. and Lee, W. S. Orbital and spin character of doped carriers in infinite-layer nickelates. *Phys. Rev. B* **104**, L220505 (2021). URL <https://link.aps.org/doi/10.1103/PhysRevB.104.L220505>.
- [39] Chen, C. T. *et al.* Electronic states in $\text{La}_{2-x}\text{Sr}_x\text{CuO}_{4+\delta}$ probed by soft-x-ray absorption. *Phys. Rev. Lett.* **66**, 104–107 (1991). URL <https://link.aps.org/doi/10.1103/PhysRevLett.66.104>.
- [40] Shen, Y. *et al.* Role of oxygen states in square planar $d^{9-\delta}$ nickelates (2021). URL <https://arxiv.org/abs/2110.08937v1>. arXiv:2110.08937.

- [41] Peng, C., Jiang, H. C., Moritz, B., Devereaux, T. P. & Jia, C. Superconductivity in a minimal two-band model for infinite-layer nickelates. *arXiv:2110.07593* (2021). URL <https://arxiv.org/abs/2110.07593>.
- [42] Lanzara, A. *et al.* Evidence for Ubiquitous Strong Electron–Phonon Coupling in High-Temperature Superconductors. *Nature* **412**, 510 (2001). URL <https://www.nature.com/articles/35087518>.
- [43] Tallon, J. L., Islam, R. S., Storey, J., Williams, G. V. M. & Cooper, J. R. Isotope Effect in the Superfluid Density of High-Temperature Superconducting Cuprates: Stripes, Pseudogap, and Impurities. *Phys. Rev. Lett.* **94**, 237002 (2005). URL <https://link.aps.org/doi/10.1103/PhysRevLett.94.237002>.
- [44] Reznik, D. *et al.* Electron–Phonon Coupling Reflecting Dynamic Charge Inhomogeneity in Copper Oxide Superconductors. *Nature* **440**, 1170 (2006). URL <https://www.nature.com/articles/nature04704>.
- [45] He, Y. *et al.* Rapid change of superconductivity and electron-phonon coupling through critical doping in Bi-2212 . *Science* **362**, 62–65 (2018). URL <https://www.science.org/doi/abs/10.1126/science.aar3394>.
- [46] He, Y. *et al.* Superconducting fluctuations in overdoped $\text{Bi}_2\text{Sr}_2\text{CaCu}_2\text{O}_{8+\delta}$. *Phys. Rev. X* **11**, 031068 (2021). URL <https://link.aps.org/doi/10.1103/PhysRevX.11.031068>.
- [47] Mishchenko, A. S. & Nagaosa, N. Electron-phonon coupling and a polaron in the t-j model: from the weak to the strong coupling regime. *Phys. Rev. Lett.* **93**, 036402 (2004). URL <https://link.aps.org/doi/10.1103/PhysRevLett.93.036402>.
- [48] Chen, Z. *et al.* Anomalously strong near-neighbor attraction in doped 1d cuprate chains. *Science* **373**, 1235–1239 (2021). URL <https://www.science.org/doi/abs/10.1126/science.abf5174>.
- [49] Wang, Y. *et al.* Phonon-mediated long-range attractive interaction in one-dimensional cuprates. *Phys. Rev. Lett.* **127**, 197003 (2021). URL <https://link.aps.org/doi/10.1103/PhysRevLett.127.197003>.
- [50] Rossi, M. *et al.* Experimental determination of momentum-resolved electron-phonon coupling. *Phys. Rev. Lett.* **123**, 027001 (2019). URL <https://link.aps.org/doi/10.1103/PhysRevLett.123.027001>.